Electronic Supplementary Material (ESI) for Energy & Environmental Science.

Supporting Information

Simultaneous interfacial chemistry engineering and inner Helmholtz plane regulating for superior alkaline hydrogen evolution

Bao Zhang[a], *Lishang Zhang*[a], *Qiuyang Tan*[b], *Jinsong Wang*[a], *Jia Liu*[a], *Houzhao Wan*[b],

Ling Miao[a], *Jianjun Jiang*[a*]

[a] School of Optical and Electronic Information, Huazhong University of Science and Technology, Wuhan 430074, China.

[b]Hubei Key Laboratory of Ferro & Piezoelectric Materials and Devices, Faculty of Physics and Electronic Science, Hubei University, Wuhan 430062, China

[*]Corresponding author: Jianjun Jiang E-mail: jiangjj@mail.hust.edu.cn

Experimental Section

Synthesis of $NiMoO_4$ on nickel foam (NF). Firstly, a piece of NF was sonicated in 6.0 M HCl for 10 min to remove the NiO layer on the top surface, then washed with ethanol and deionized water, respectively, and dried in air. $NiMoO_4$ precursor were synthesized by a hydrothermal method. Typically, 2.4 mmol $Ni(NO_3)_2•6H_2O$ and 0.6 mmol $(NH_4)_6Mo_7O_{24}•xH_2O$ were dissolved in 60 mL deionized water. After gentle stirring for 30 min, the solution was then transferred to a 80 mL Teflon-lined stainless steel autoclave with a piece of NF (2 cm × 4 cm). The autoclave was sealed and heated at 150 °C for 6 h in an oven and then cooled down to room temperature naturally. Finally, the product was taken out, rinsed with deionized water and ethanol several times and dried at 60 °C in air.

Synthesis of Ni-Mo-N. The prepared $NiMoO_4$ precursor was nitrided in a tube furnace system at various temperature (from 350 °C to 450 °C) for 3h under the high purity NH_3 atmosphere. The best Ni-Mo-N was prepared under 400 °C, named $Ni_{0.2}Mo_{0.8}N/Ni$.

Synthesis of $Ni_{0.2}Mo_{0.8}N$. The prepared $Ni_{0.2}Mo_{0.8}N/Ni$ at 400 °C was immersed in 2M HCl for 2 h and taken out, then rinsed with deionized water and ethanol several times and dried at 60 °C in air.

Synthesis of porous Ni. The electrodeposition of porous Ni was carried out in a standard three electrode electrochemical cell (NF, working electrode; Pt foil, counter electrode; Ag/AgCl, reference electrode). The electrolyte was an aqueous solution of 0.1 M $NiCl_2$ and 1 M NH_4Cl. The electrodeposition experiments were all carried out at a constant cathodic current density of 1 A cm^{-2} for 500 s. After the deposition, the obtained electrode was taken out, rinsed with deionized water and ethanol several times and dried at 60 °C in air.

Synthesis of NiFe-LDH. NiFe-LDH was synthesized via a hydrothermal method. Firstly, a piece of NF was pretreated and dried. Typically, 3 mmol $Ni(NO_3)_2•6H_2O$, 1 mmol $Fe(NO_3)_3•9H_2O$ and 5 mmol urea were dissolved in 60 mL deionized water. After gentle stirring for 30 min, the solution was then transferred to a 80 mL Teflon-lined stainless steel autoclave with a piece of NF (2 cm × 4 cm). The autoclave was sealed and heated at 120 °C for 12 h in an oven and then cooled down to room temperature naturally. Finally, the product was taken out, rinsed with deionized water and ethanol several times and dried at 60 °C in air.

Materials Characterization. The morphology and the structure of the electrodes were characterized by a field emission scanning electron microscopy (SEM; Gemini SEM 300). TEM images were obtained from JEM 2100F. Powder X-ray diffraction (XRD) patterns were acquired on a Philips X'Pert PRO with Cu Kα radiation, λ = 1.5418Å. The X-ray photoelectron spectroscopy (XPS) spectra were measured on Kratos AXIS Ultra DLD-600W XPS system equipped with a monochromatic Al K (1486.6 eV) as X-ray source.

Electrochemical Measurements. All the electrochemical measurements were conducted using a CHI760E potentiostat (CH Instruments, China) in a typical three electrode setup, with a piece of freshly-made electrode as the working electrode, a carbon rod as the counter electrode and Ag/AgCl electrode as the reference electrode. Prior to every measurement, a resistance test was made and the iR compensation was applied to all initial data for further analysis. LSV measurements were conducted at a scan rate of 2 mV s^{-1} at room temperature in 1.0 M KOH electrolyte and 0.5M H_2SO_4 electrolyte. All polarization curves were iR-corrected unless noted. All the potentials were calibrated with respect to RHE by the equation E(RHE) = E(Ag/AgCl) + 0.198 V + 0.059V*pH. EIS measurements were carried out in the frequency range of 100 kHz–0.1Hz at potential of 100 mV versus RHE.

MD simulations. The molecular dynamics (MD) simulation to study the electrochemical double layer structures (EDL) by using LAMMPS[1]. The model contains two NiMoN slabs, one Ni nanoparticles and 1M KOH electrolyte. The properties of H_2O are assessed with SPC/E. The force-fields parameters of K^+ , OH^-, Ni, Mo and N are taken from cvff and opls forcefield. The systems are setup initially by using PACKMOL[2] and Moltemplate (http://www.moltemplate.org/). Firstly, a 1 ns NPT run are performed to ensure the equilibrium. Then a 5 ns NVT run is performed at 300 K. The last 3 ns trajectory is used to obtain the structure of EDL. The charges of NiMoN slab and Ni nanoparticle are assigned with charge density of 1 uC/cm^2 and 10 uC/cm^2, respectively. And they are both fixed during the MD simulations.

DFT Calculations. The DFT calculations[3,4] are performed by using Vienna Ab-initio Simulation Package (VASP)[5] with Projector Augmented Wave (PAW) method[6]. And the exchange-correlation energy is described by the functional of Perderw, Burke, and Ernzerhof (PBE) form[7,8]. The kinetic energy cutoff of electron wave functions is 500 eV. The geometry optimizations are performed by using the conjugated gradient method, and the convergence threshold is set to be 10^{-4} eV in energy and 0.05 eV $Å^{-1}$ in force. A vacuum layer of 15 Å is applied for all calculated models, and one layer of water molecules is employed to account for solvation effect. The Brillouin zone is sampled by using the Monkhorst−Pack scheme[9]. The free energy of hydroxyl adsorption on are defined as:

$$\Delta G_{OH} = G_{sur\text{-}OH} - G_{sur} - G_{OH^-}$$

where $G_{sur\text{-}OH}$, G_{OH}, and G_{sur} are the free energies of species adsorbed, hydroxyl species and clean surfaces, respectively. At equilibrium potential of HER:

$$G_{H_2O} = G_{OH^-} + \frac{1}{2} G_{H_2}$$

Thus,

$$\Delta G_{OH} = G_{sur\text{-}OH} - G_{sur} - G_{H_2O} + \frac{1}{2} G_{H_2}$$

TS values are from previous report [10]:

$$\Delta G_{OH} = E_{sur\text{-}OH} - E_{sur} - E_{H_2O} + \frac{1}{2} E_{H_2} + 0.29\ eV$$

The solvent induced polarization charge is calculated based on PWmat code[11,12] with similar setup. Visualization of the atomic structures are made by using VESTA[13]. Herein, four main steps in alkaline HER are considered: water adsorption and activation, H* intermediates formation, H_2 formation.[14]

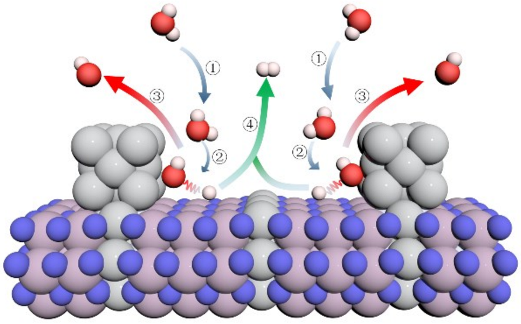

Figure S1. Schematic illustration of bifunctional-mode alkaline HER mechanism.

As shown in Fig.S1, the key reaction steps and related free energies (at the reduction potentials U_0=0 V vs RHE) are calculated as:

①
$$H_2O \rightarrow H_2O^*$$
$$\Delta G_1 = G_{H_2O^*} - G_{H_2O}$$

②
$$H_2O^* \rightarrow H^* + OH^*$$
$$\Delta G_2 = G_{H^*} + G_{OH^*} - G_{H_2O^*}$$

③
$$H^* + OH^* + e^- \rightarrow H^* + OH^-$$
$$\Delta G_3 = -G_{OH^*}$$

④ $H^* \rightarrow \frac{1}{2}H_2$

$$\Delta G_3 = -G_{H^*}$$

The free energy diagrams were calculated using the equation:

$$G = E + ZPE - TS$$

where *G, E, ZPE* and *TS* are the free energy, total energy from DFT calculations, zero point energy and entropic contributions (T was set to be 300K), respectively. *ZPE* could be derived after frequency calculation by:

$$ZPE = \frac{1}{2}\sum hv_i$$

The *TS* values of adsorbed species are calculated after obtaining the vibrational frequencies[15]:

$$TS_v = k_B T\left[\sum\nolimits_K \ln\left(\frac{1}{1-e^{-hv/\mathrm{k}_B T}}\right) + \sum\nolimits_K \frac{hv}{k_B T}\frac{1}{(e^{hv/\mathrm{k}_B T}-1)} + 1\right]$$

Kinetics Analysis:

Following the procedure of Wang et al.,[16] dual-pathway kinetics analysis is performed to evaluate the standard activation free energies for the three elementary reaction steps of HER.

$$\mathrm{j}_T = j^* e^{-\Delta G_T^{*0}/kT}[(1-\theta)^2 - e^{2\Delta G_H/kT}\theta^2]$$

$$\mathrm{j}_H = j^* e^{-\Delta G_H^{*0}/kT}[(1-\theta)e^{0.5\eta/kT} - e^{(\Delta G_H - 0.5\eta)/kT}\theta]$$

$$\mathrm{j}_V = 2j^* e^{-\Delta G_V^{*0}/kT}[(\theta e^{(\Delta G_H + 0.5\eta)/kT} - e^{-0.5\eta/kT}\theta]$$

Where j*, θ, ΔG_i^{*0} is the reference prefactor, the adsorption isotherm,□and the standard activation free energy, respectively (ΔG_V^{*0} for Volmer step, ΔG_T^{*0} for Tafel step, and ΔG_H^{*0} for Heyrovsky step).

θ can be given below:

$$\theta = \frac{-B - \sqrt{B^2 - 4AC}}{2A}$$

where

$$A = 2\mathrm{g}_{+T} - 2\mathrm{g}_{-T}$$

$$B = -4\mathrm{g}_{+T} - 2\mathrm{g}_{+H} - \mathrm{g}_{-H} - \mathrm{g}_{+V} - \mathrm{g}_{-V}$$

$$C = 2\mathrm{g}_{+T} + \mathrm{g}_{+H} + \mathrm{g}_{-V}$$

and

$$g_{+T}=e^{-\Delta G_T^{*0}/kT}$$

$$g_{-T}=e^{-(G_T^{*0}-2\eta)/kT}$$

$$g_{+H}=e^{-(G_H^{*0}-0.5\eta)/kT}$$

$$g_{-H}=e^{-(G_H^{*0}-G_H+0.5\eta)/kT}$$

$$g_{+V}=e^{-(G_V^{*0}-G_H-0.5\eta)/kT}$$

$$g_{-V}=e^{-(G_V^{*0}+0.5\eta)/kT}$$

We can fit the polarization curves by ΔG_H and $\Delta G0^*$ X.

The Ni nanoparticles are loaded on the NiMoN/Ni surface. After etching the Ni, a rugged NiMoN surface is displayed (Figure S3c-d). Therefore, Ni nanoparticles are partially embedded in the $Ni_{0.2}Mo_{0.8}N$ matrix. As shown in Figure S5, the Ni nanoparticles have similar size under nitridation temperature of 400℃ and 450℃ (10~15 nm). The densities of Ni particles are different at different surface. At the top, nitridation temperature of 400℃ leads to a large density of Ni nanoparticles about ~1370/um^2, which larger than that of 450℃. In contrast, the density of Ni nanoparticles at side surface almost stays the same of 450℃. Besides, the XRD patterns indicate a higher crystallinity under 450℃. Therefore, the topmost Ni nanoparticles density and the crystallinity maybe result in the different HER activities under nitridation temperature of 400℃ and 450℃ (Figure S9).

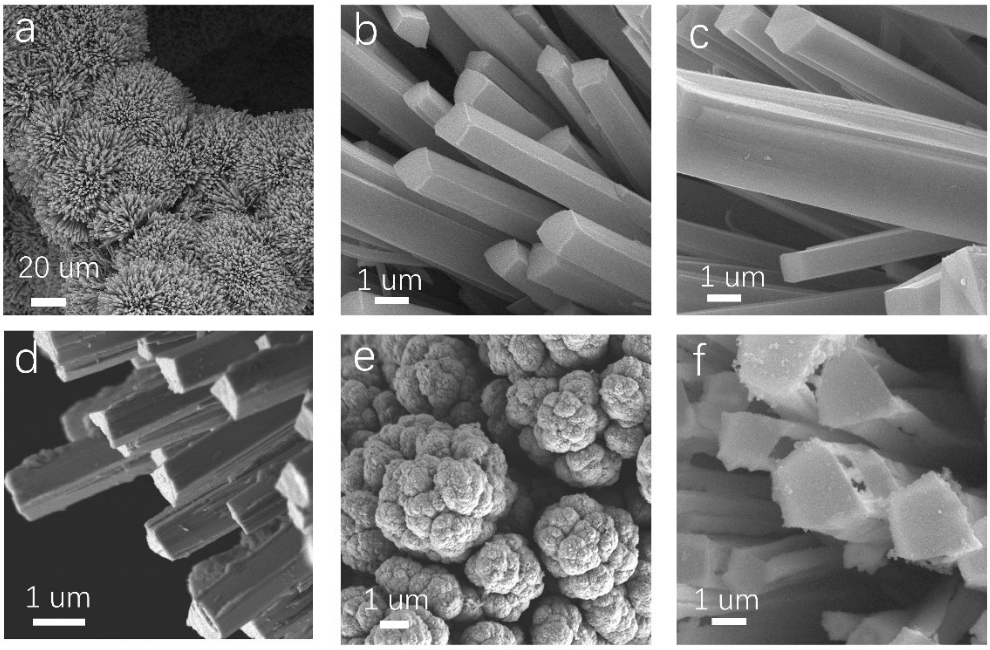

Figure S2. SEM images of: a-b) NiMoN/Ni-400, c) NiMoN/Ni -450 °C, d) NiMoN/Ni -350 °C, e) porous Ni, f) NiMoN.

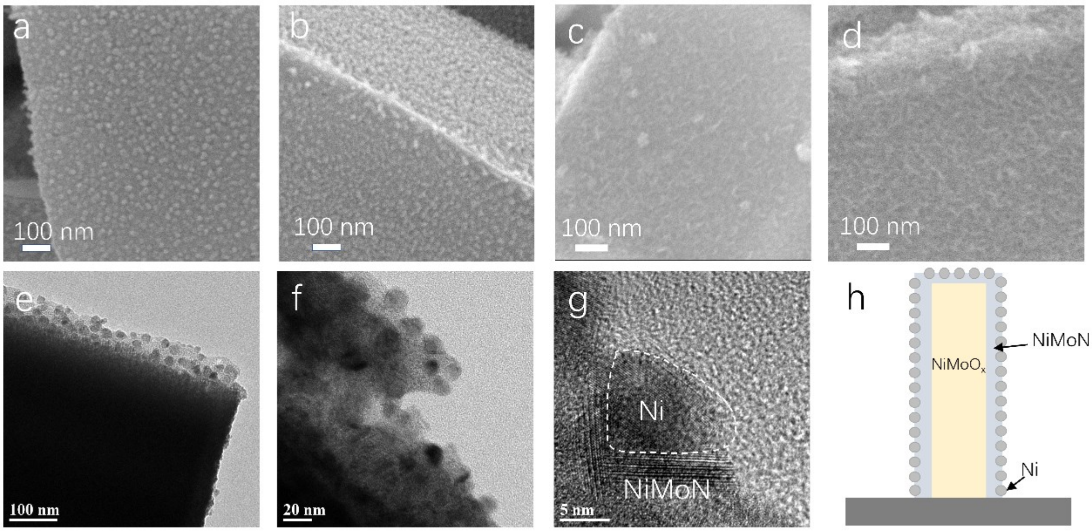

Figure S3. SEM images of: a-b) NiMoN/Ni-400, c-d) NiMoN. e-g) TEM images of NiMoN/Ni-400. h) Schematic diagram of this NiMoN/Ni structure.

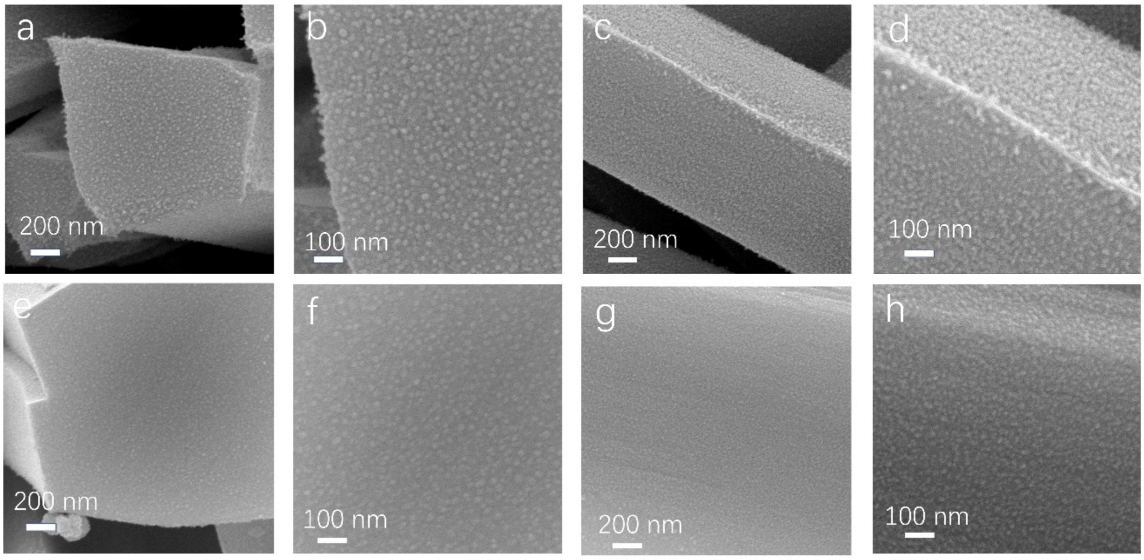

Figure S4. SEM images of NiMoN/Ni. a-b) top view of NiMoN/Ni-400, c-d) side view of NiMoN/Ni-400, e-f) top view of NiMoN/Ni-450, g-h) side view of NiMoN/Ni-450.

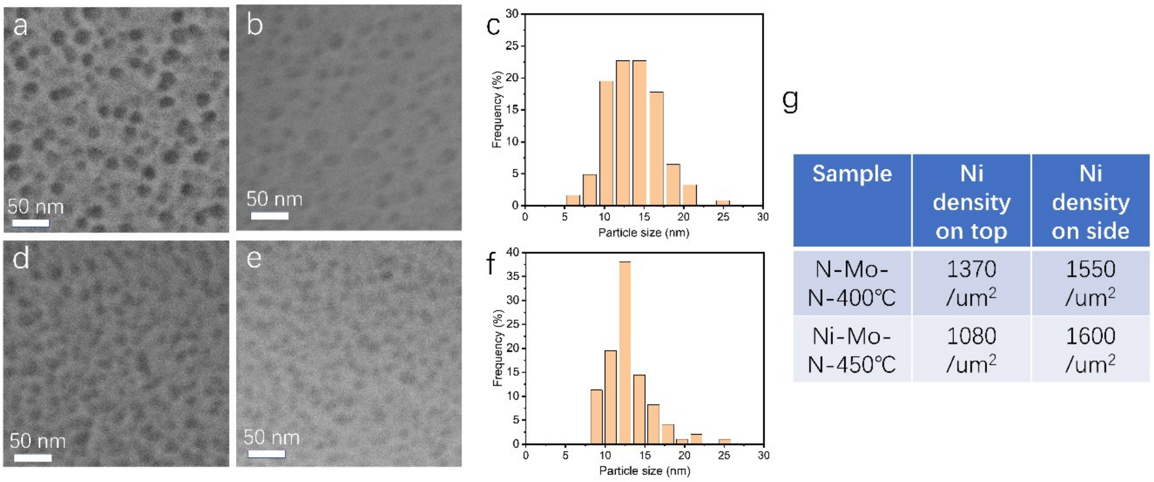

Sample	Ni density on top	Ni density on side
N-Mo-N-400℃	1370 /um^2	1550 /um^2
Ni-Mo-N-450℃	1080 /um^2	1600 /um^2

Figure S5. Phase reversal SEM images, particle size distribution and densities of Ni. a) top view of NiMoN/Ni-400, b) side view of NiMoN/Ni-400, c) particle size distribution of NiMoN/Ni-400, d) top view of NiMoN/Ni-450, e) side view of NiMoN/Ni-450, f) particle size distribution of NiMoN/Ni-400, g) Ni densities on top and side surfaces.

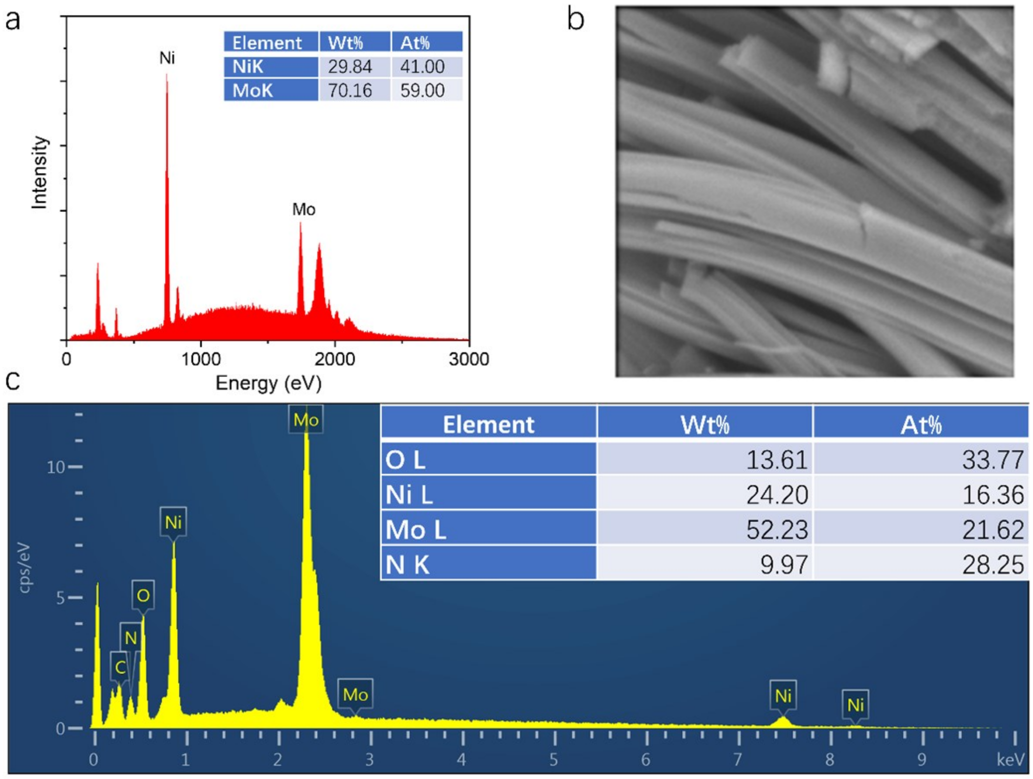

Element	Wt%	At%
NiK	29.84	41.00
MoK	70.16	59.00

Element	Wt%	At%
O L	13.61	33.77
Ni L	24.20	16.36
Mo L	52.23	21.62
N K	9.97	28.25

Figure S6. Chemical composition analyses a) XRF and EDS analyses of NiMoN/Ni.

The composition of Ni$_{0.2}$Mo$_{0.8}$N/Ni is further analysed by EDS and XRF. The XRF analysis confirms that the Ni-Mo-N power consists of Ni and Mo elements, and the molar ratio of Ni to Mo is about 1.13:1. The EDS analyses demonstrates that the Ni-Mo-N power consists of Ni, Mo, N and O elements, which is consistent with XPS data. The Ni/Mo/N molar ratio is about 1:1.32:1.73. The Mo:N molar ratio is about 0.76, which is close to theoretical ratio of $Ni_{0.2}Mo_{0.8}N$.

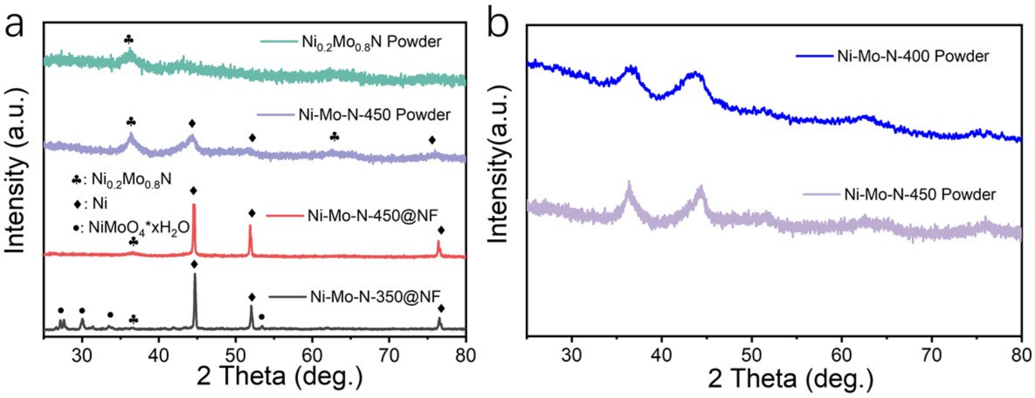

Figure S7. XRD patterns of as-prepared nitrides.

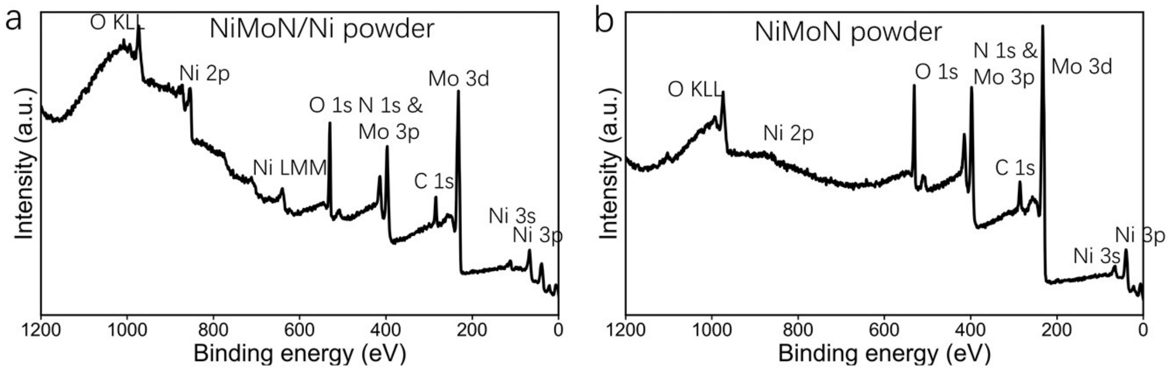

Figure S8. XPS survey of NiMoN/Ni and NiMoN.

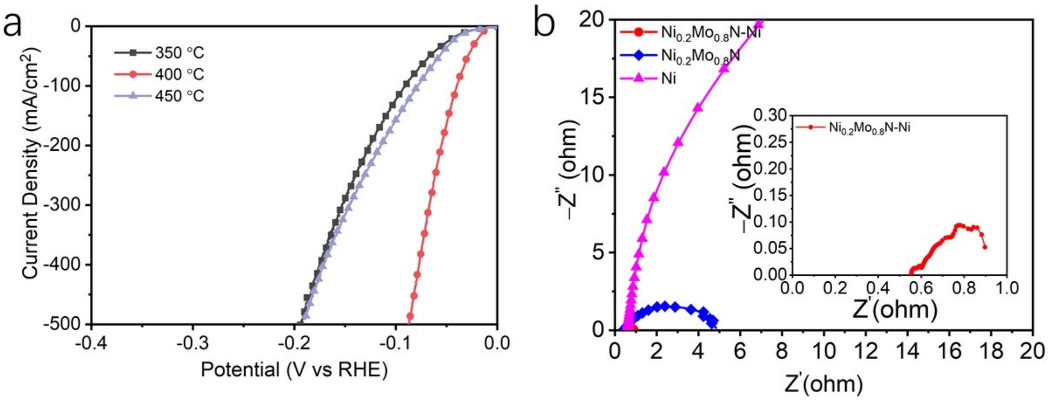

Figure S9. (a)LSV curves of Ni-Mo-N under various nitridation temperature. (b)EIS curves under 100 mV *vs*. RHE

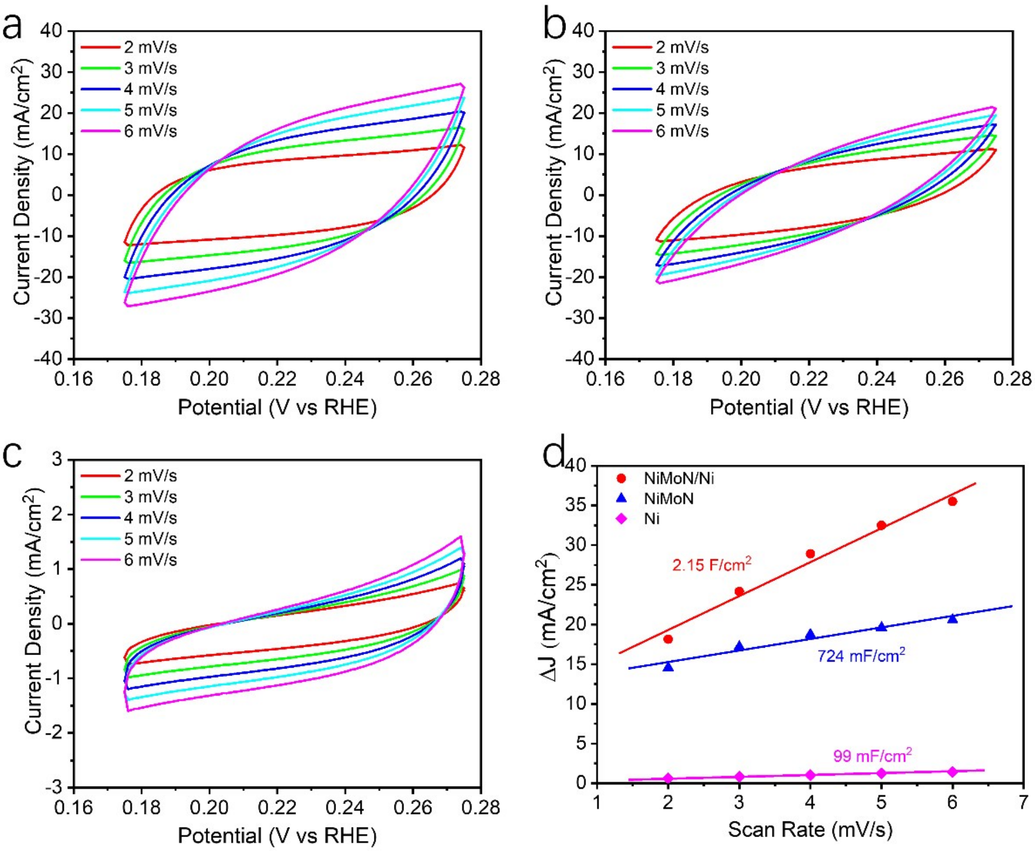

Figure S10. Cyclic voltammogram curves of a) NiMoN/Ni, b) NiMoN, and c) Ni in the double layer capacitive region at the scan rates of from 2 mV/s to 6 mV/s. d) Calculated double layer capacitance.

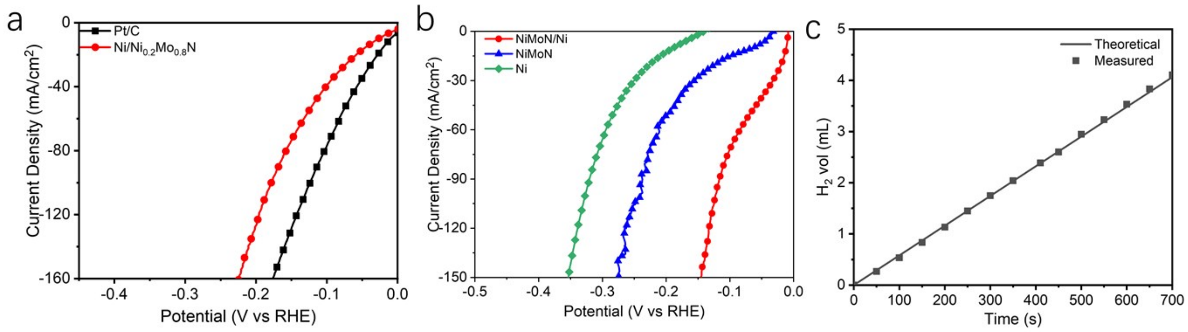

Figure S11. a) The intrinsic HER activity of NiMoN/Ni powders (~1 mg/cm^2). b) Polarization curves in 0.5M H_2SO_4. c) Amount of hydrogen theoretically calculated and experimentally measured versus time for NiMoN/Ni in 1M KOH.

It's generally accepted that the acidic HER performance is mainly determined by the H* adsorption free energies. The polarization curves in 0.5M H_2SO_4 are shown in Figure S11a. The Ni exhibits lowest acidic HER activity among them, indicating a too week or too strong H* adsorption. The NiMoN/Ni exhibits higher acidic HER activity than that of NiMoN, suggesting an improved H* adsorption free energies on NiMoN/Ni hybrid catalyst.

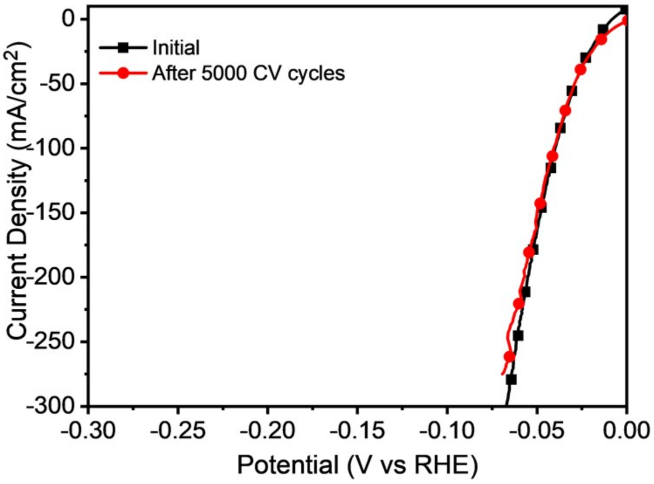

Figure S12. Polarization curves after 5000 CV cycles (0~100 mV *vs.* RHE, 50 mV/s)

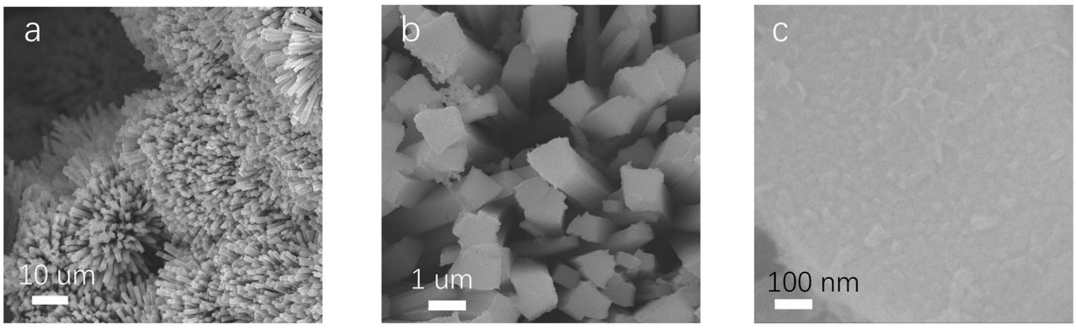

Figure S13. The SEM image of NiMoN/Ni after 5000 CV cycling test.

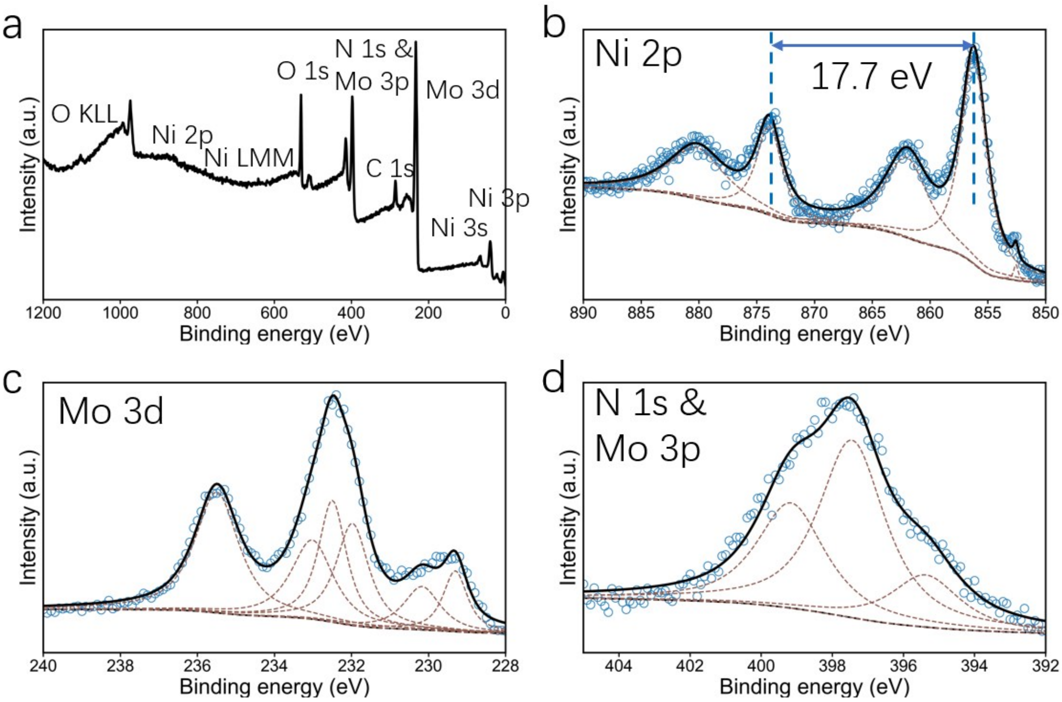

Figure S14. The XPS spectra of of NiMoN/Ni after cycling test.

After 5000 CV stability test, the NiMoN/Ni major heterostructure remains unchanged, while some new nanosheets appear on the surface (Figure S13). The Ni 2p XPS spectrum shows two major peaks centered around 856.2 and 873.9 eV with a spin-energy separation of 17.7 eV, corresponding to Ni $2p_{1/2}$ and Ni $2p_{3/2}$, respectively, which is the characteristic of $Ni(OH)_2$ phase[17]. These indicate that the surface Ni nanoparticles and NiMoN are partly converted to $Ni(OH)_2$ during CV test in alkaline environment as demonstrated by Sargent's group and Dai's group[18,19]. The $Ni(OH)_2$ can also act as a water-dissociation promoter[17]. Therefore, the HER activity is basically maintained even for 5000 CV cycles. The Ni:Mo:N atomic ratio from XPS data is about 1:0.45:1. Compared to the initial catalyst (1:1.32:1.73), the Mo and N atomic ratio decreased. The Mo^{6+} species oxidized by oxygen in the electrolyte can be dissolved in alkaline solution during the CV test, leading to the decreasing of Mo and N[20].

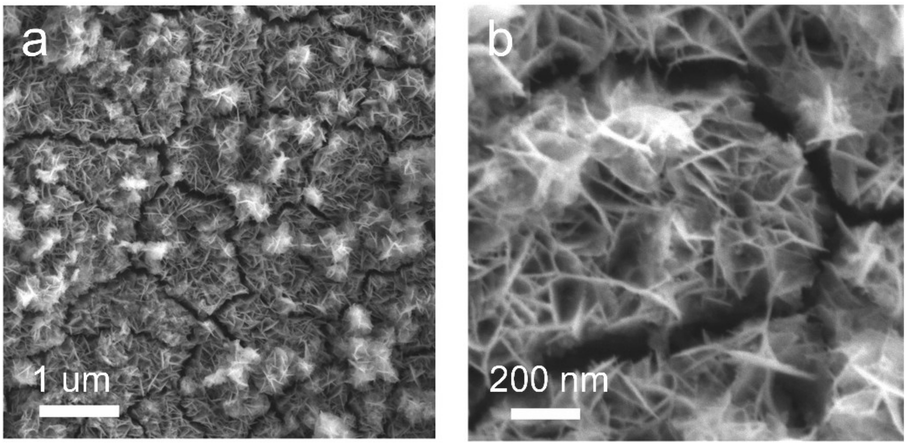

Figure S15. The SEM images of NiFe-LDH.

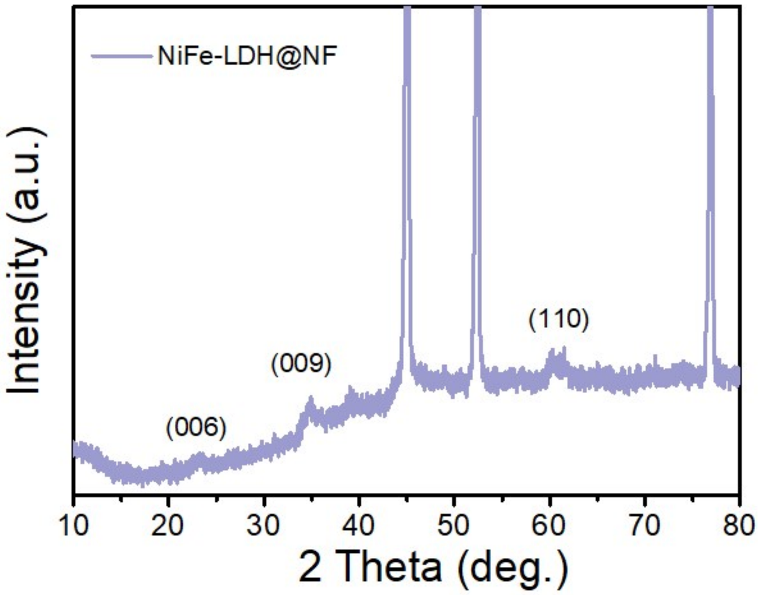

Figure S16. XRD pattern of NiFe-LDH.

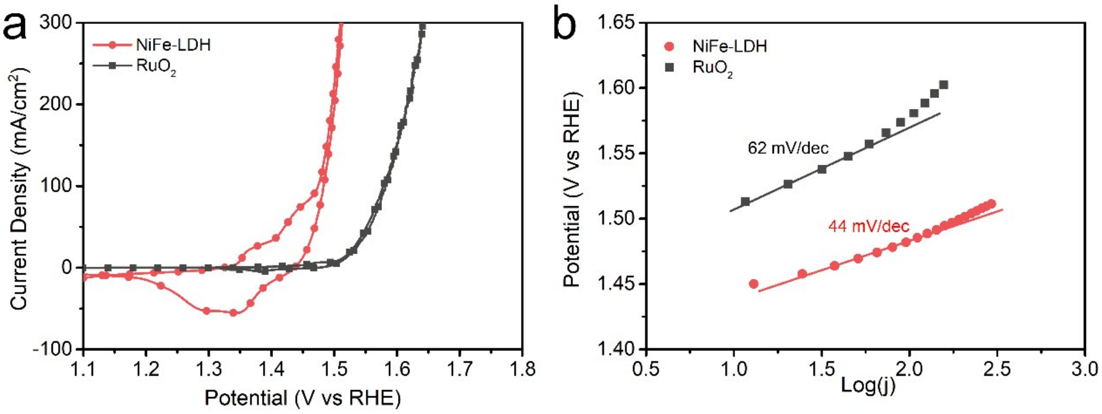

Figure S17. a) CV curves and b) Tafel plots of NiFe-LDH and RuO_2.

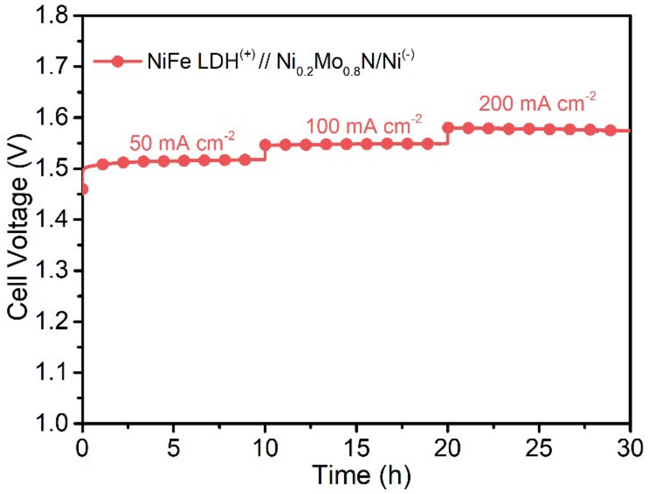

Figure S18. Long-term durability for overall watersplitting with NiFe LDH as anode and NiMoN/Ni as cathode.

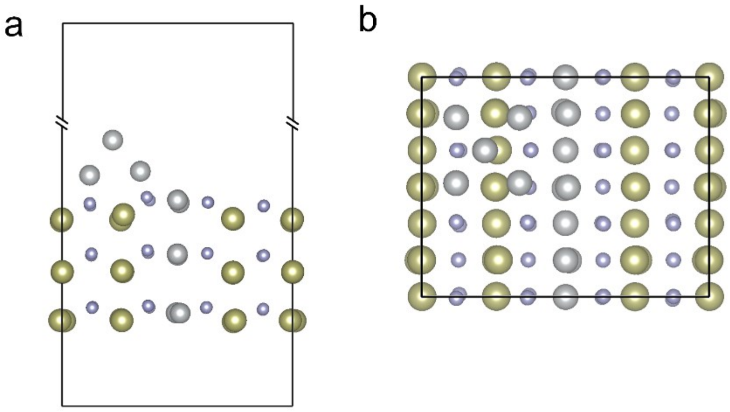

Figure S19. The structural models of the NiMoN/Ni catalysts. The Mo, Ni, N atoms are represented by light yellow, gray and light blue spheres, respectively.

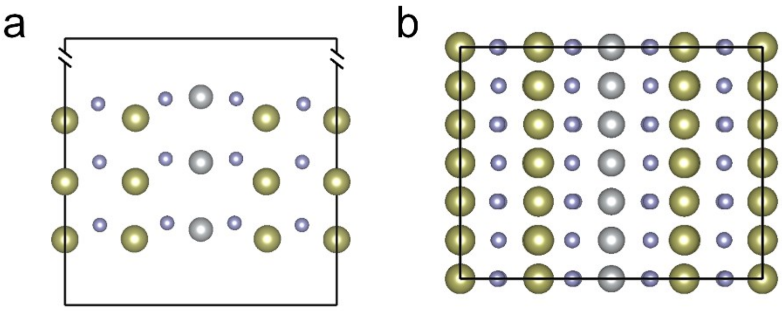

Figure S20. The structural models of the NiMoN catalysts.

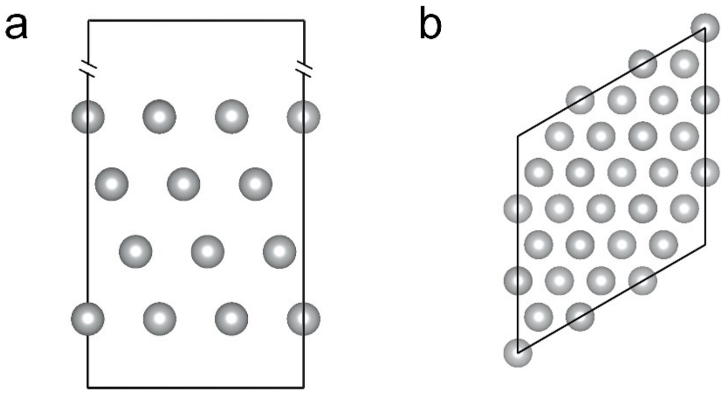

Figure S21. The structural models of the Ni catalysts.

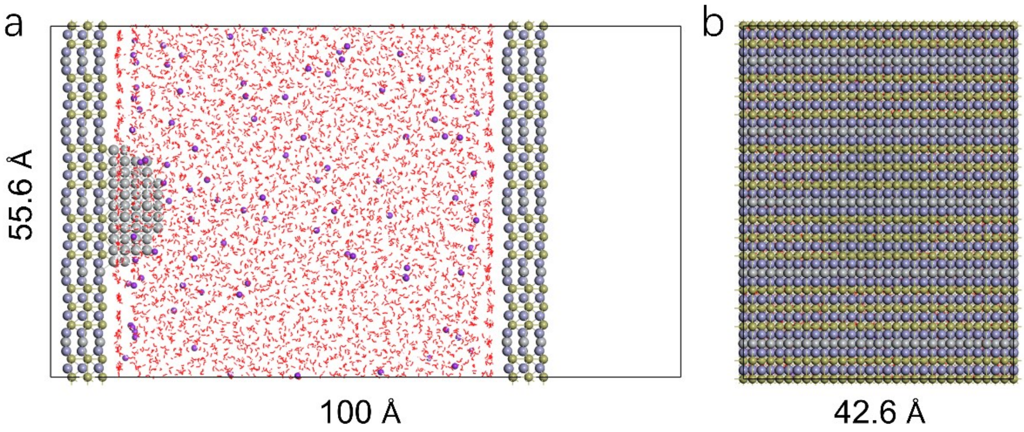

Figure S22. The structural models of the MD simulations.

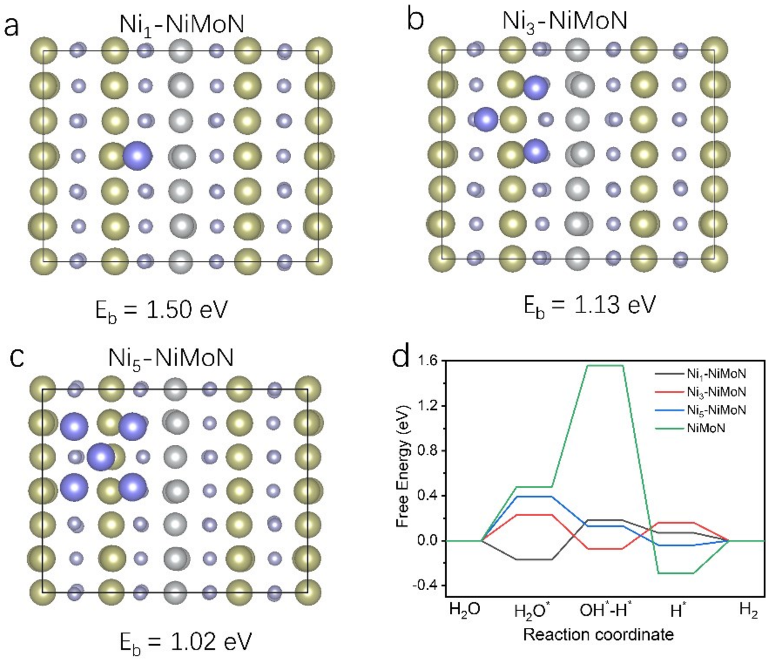

Figure S23. Ni$_n$-NiMoN DFT models and corresponding HER mechanism.

The use of different number of Ni particles in modeling may affect the pathways of associative mechanism. As the reviewer suggests, various Ni_n (n=1,3,5) clusters are tested according to the reference[21]. The formation energies per Ni atom with respect to bulk Ni are 1.50, 1.13 and 1.02 eV for Ni_1, Ni_3 and Ni_5 clusters, respectively. The Ni_3 and Ni_5 clusters are more stable than Ni_1. Further HER mechanism calculations are carried out. As shown in **Fig. R5**, demonstrate that all these Ni_n clusters can act as a good water activation promoter, and the water activation barriers of Ni_n-NiMoN are all dramatically decreased compared to NiMoN. These confirm the interfacial synergy effect between Ni and NiMoN.

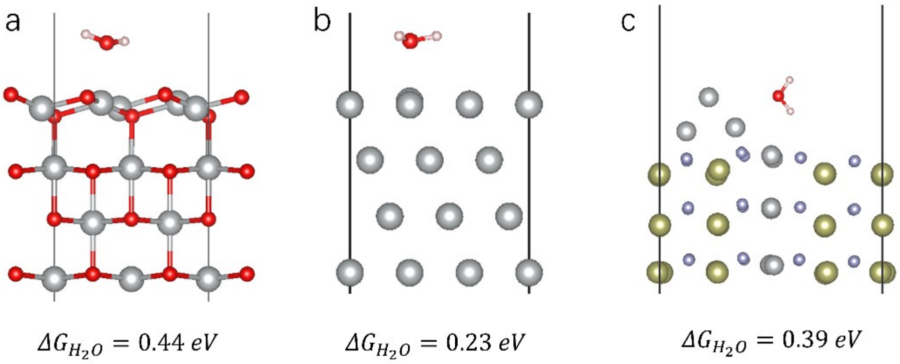

$\Delta G_{H_2O} = 0.44\ eV$ $\Delta G_{H_2O} = 0.23\ eV$ $\Delta G_{H_2O} = 0.39\ eV$

Figure S24. The water adsorption model and corresponding adsorption free energies on a)NiO, b)Ni, and c)Ni_5-NiMoN.

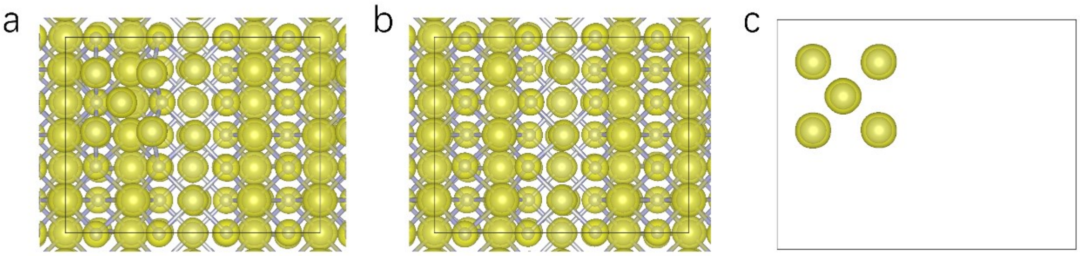

Figure S25. The charge density isosurfaces (0.25 *e* $Bohr^{-3}$) of a) Ni-NiMoN, b)NiMoN, c)Ni_5 clusters.

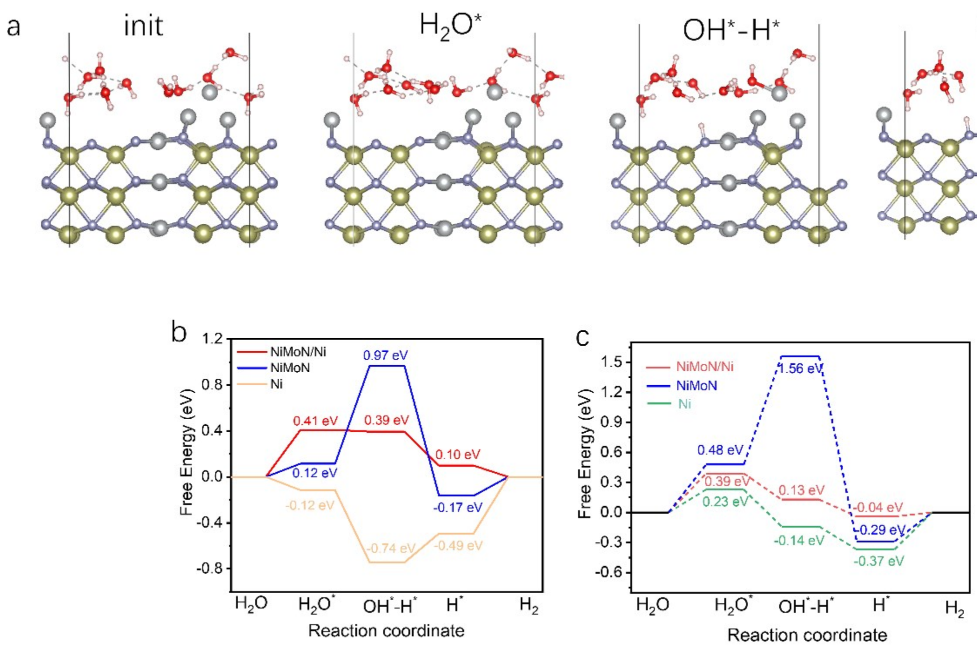

Figure S26. a) Explicit solvation model. DFT calculated free energy diagrams of b) explicit solvation model and c) simple model.

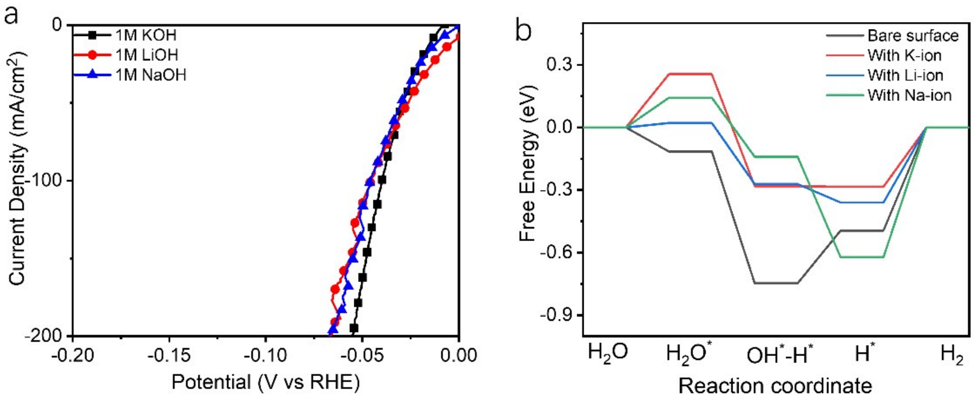

Figure S27. a) Polarization curves in 1M KOH, LiOH and NaOH. b) Free energy diagrams of Ni (111) with surface-adsorbed Alkali-ion.

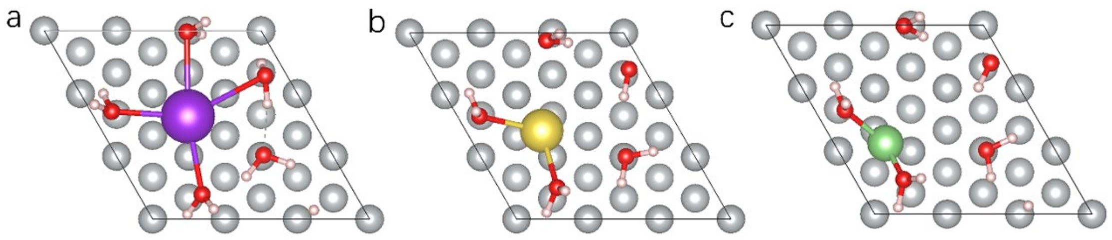

Figure S28. DFT models of alkali-ion on Ni surface: a) K-ion, b) Na-ion, and c) Li-ion. And there bader charges are +0.89, +0.90, and +0.87, respectively.

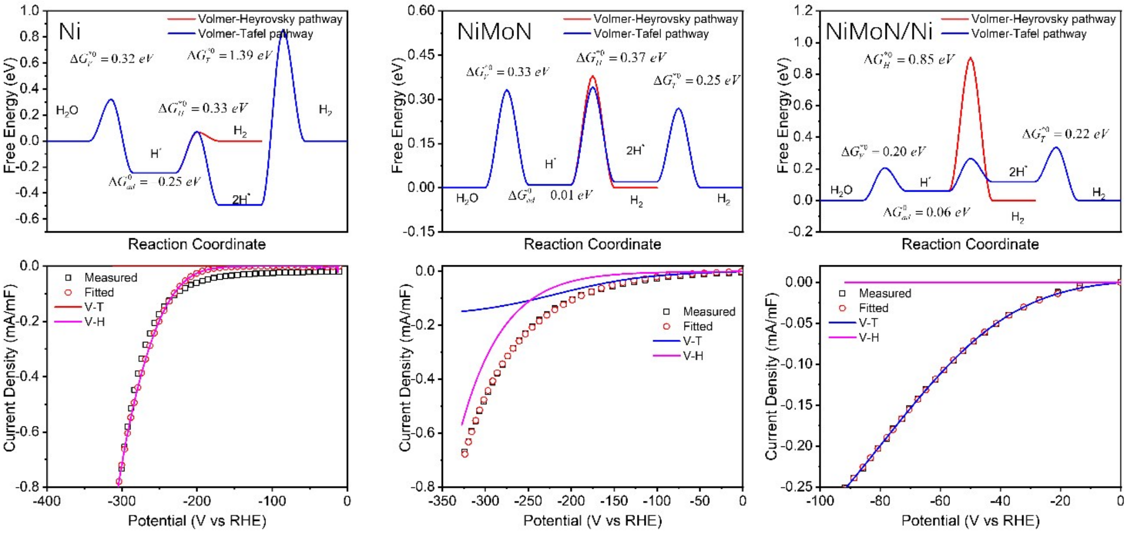

Figure S29. a-f) ECSA normalized polarization curves and the fits using the dual-pathway microkinetic model and related free energy diagrams.

Table S1. The alkaline HER activities of the $Ni_{0.2}Mo_{0.8}N/Ni$ and the reported non-noble based electrocatalysts

Electrocatalysts	Overpotential at 10 mA cm^{-2}	Tafel slope (mV dec^{-1})	Reference
$Ni_{0.2}Mo_{0.8}N/Ni$	14	33	This work
Ni_3FeN	45	75	22
V_8C_7	47	44.5	23
NiMoN	109	95	24
Se-(NiCo)S/OH	1101	87.3	25
$Ni(OH)_2/MoS_2$	80	60	14
$CoP/Ni_5P_4/CoP$	71	58	26
Ni-S-Se	112	94.1	27
$Ni-N_{0.19}$	42	125	28
$Cu-Ni_3S_2$	128	76.2	29
NiCoP	42	90	30

Table S2. The alkaline watersplitting activities of NiFe LDH$^{(+)}$//$Ni_{0.2}Mo_{0.8}N$/Ni$^{(-)}$ coupled electrolyzer and the reported electrolyzer

Electrolyzer	Cell voltages at 100 mA/cm^2	Reference
NiFe LDH$^{(+)}$//$Ni_{0.2}Mo_{0.8}N$/Ni$^{(-)}$	1.52	This work
NiFe-CuNWs$^{(+)}$// NiFe-CuNWs$^{(-)}$	1.69	31
Co-P$^{(+)}$ //Co-P$^{(-)}$	1.74	32
NiCoP-CC $^{(+)}$ // NiCoP-CC$^{(-)}$	1.77	33
NiFe LDH$^{(+)}$//Ni@NiO/$Cr_2O_3$$^{(-)}$	1.53	34
NiFe LDH$^{(+)}$//Ni-NiO$^{(-)}$	1.58	35
CoFeP$^{(+)}$//CoFeP$^{(-)}$	1.61	36

Reference:

(1) Plimpton, S. Fast Parallel Algorithms for Short-Range Molecular Dynamics. *Journal of computational physics* **1995**, *117* (1), 1–19.

(2) Martínez, L.; Andrade, R.; Birgin, E. G.; Martínez, J. M. PACKMOL: A Package for Building Initial Configurations for Molecular Dynamics Simulations. *Journal of computational chemistry* **2009**, *30* (13), 2157–2164.

(3) Hohenberg, P.; Kohn, W. Inhomogeneous Electron Gas. *Physical review* **1964**, *136* (3B), B864.

(4) Kohn, W.; Sham, L. J. Self-Consistent Equations Including Exchange and Correlation Effects. *Physical review* **1965**, *140* (4A), A1133.

(5) Kresse, G.; Hafner, J. Ab Initio Molecular Dynamics for Liquid Metals. *Physical Review B* **1993**, *47* (1), 558.

(6) Blöchl, P. E. Projector Augmented-Wave Method. *Physical review B* **1994**, *50* (24), 17953.

(7) Kresse, G.; Furthmüller, J. Efficient Iterative Schemes for Ab Initio Total-Energy Calculations Using a Plane-Wave Basis Set. *Physical review B* **1996**, *54* (16), 11169.

(8) Perdew, J. P.; Burke, K.; Ernzerhof, M. Generalized Gradient Approximation Made Simple. *Physical review letters* **1996**, *77* (18), 3865.

(9) Monkhorst, H. J.; Pack, J. D. Special Points for Brillouin-Zone Integrations. *Physical review B* **1976**, *13* (12), 5188.

(10) Pham, H. H.; Cheng, M.-J.; Frei, H.; Wang, L.-W. Surface Proton Hopping and Fast-Kinetics Pathway of Water Oxidation on Co3O4 (001) Surface. *ACS Catal.* **2016**, *6* (8), 5610–5617. https://doi.org/10.1021/acscatal.6b00713.

(11) Jia, W.; Cao, Z.; Wang, L.; Fu, J.; Chi, X.; Gao, W.; Wang, L.-W. The Analysis of a Plane Wave Pseudopotential Density Functional Theory Code on a GPU Machine. *Computer Physics Communications* **2013**, *184* (1), 9–18.

(12) Jia, W.; Fu, J.; Cao, Z.; Wang, L.; Chi, X.; Gao, W.; Wang, L.-W. Fast Plane Wave Density Functional Theory Molecular Dynamics Calculations on Multi-GPU Machines. *Journal of Computational Physics* **2013**, *251*, 102–115.

(13) Momma, K.; Izumi, F. VESTA 3 for Three-Dimensional Visualization of Crystal, Volumetric and Morphology Data. *Journal of applied crystallography* **2011**, *44* (6), 1272–1276.

(14) Zhang, B.; Liu, J.; Wang, J.; Ruan, Y.; Ji, X.; Xu, K.; Chen, C.; Wan, H.; Miao, L.; Jiang, J. Interface Engineering: The Ni(OH)2/MoS2 Heterostructure for Highly Efficient Alkaline Hydrogen Evolution. *Nano Energy* **2017**, *37*, 74–80. https://doi.org/10.1016/j.nanoen.2017.05.011.

(15) Bendavid, L. I.; Carter, E. A. CO2 Adsorption on Cu2O (111): A DFT+ U and DFT-D Study. *The Journal of Physical Chemistry C* **2013**, *117* (49), 26048–26059.

(16) Wang, Jia. X.; Springer, T. E.; Liu, P.; Shao, M.; Adzic, R. R. Hydrogen Oxidation Reaction on Pt in Acidic Media: Adsorption Isotherm and Activation Free Energies. *The Journal of Physical Chemistry C* **2007**, *111* (33), 12425–12433. https://doi.org/10.1021/jp073400i.

(17) Zhang, B.; Liu, J.; Wang, J.; Ruan, Y.; Ji, X.; Xu, K.; Chen, C.; Wan, H.; Miao, L.; Jiang, J. Interface Engineering: The Ni(OH)2/MoS2 Heterostructure for Highly Efficient Alkaline Hydrogen Evolution. *Nano Energy* **2017**, *37*, 74–80. https://doi.org/10.1016/j.nanoen.2017.05.011.

(18) Gong, M.; Zhou, W.; Kenney, M. J.; Kapusta, R.; Cowley, S.; Wu, Y.; Lu, B.; Lin, M.-C.; Wang, D.-Y.; Yang, J.; Hwang, B.-J.; Dai, H. Blending Cr2O3 into a NiO–Ni Electrocatalyst for Sustained Water Splitting. *Angewandte Chemie International Edition* **2015**, *54* (41), 11989–11993. https://doi.org/10.1002/anie.201504815.

(19) Dinh, C.-T.; Jain, A.; de Arquer, F. P. G.; De Luna, P.; Li, J.; Wang, N.; Zheng, X.; Cai, J.; Gregory, B. Z.; Voznyy, O.; Zhang, B.; Liu, M.; Sinton, D.; Crumlin, E. J.; Sargent, E. H. Multi-Site Electrocatalysts for Hydrogen Evolution in Neutral Media by Destabilization of Water Molecules. *Nature Energy* **2019**, *4* (2), 107–114. https://doi.org/10.1038/s41560-018-0296-8.

(20) Li, Y.; Wei, X.; Chen, L.; Shi, J.; He, M. Nickel-Molybdenum Nitride Nanoplate Electrocatalysts for Concurrent Electrolytic Hydrogen and Formate Productions. *Nature Communications* **2019**, *10* (1), 5335. https://doi.org/10.1038/s41467-019-13375-z.

(21) Liu, J.-C.; Ma, X.-L.; Li, Y.; Wang, Y.-G.; Xiao, H.; Li, J. Heterogeneous Fe 3 Single-Cluster Catalyst for Ammonia Synthesis via an Associative Mechanism. *Nature Communications* **2018**, *9* (1), 1610. https://doi.org/10.1038/s41467-018-03795-8.

(22) Wang, Y.; Xie, C.; Liu, D.; Huang, X.; Huo, J.; Wang, S. Nanoparticle-Stacked Porous Nickel–Iron Nitride Nanosheet: A Highly Efficient Bifunctional Electrocatalyst for Overall Water Splitting. *ACS Applied Materials & Interfaces* **2016**, *8* (29), 18652–18657. https://doi.org/10.1021/acsami.6b05811.

(23) Xu, H.; Wan, J.; Zhang, H.; Fang, L.; Liu, L.; Huang, Z.; Li, J.; Gu, X.; Wang, Y. A New Platinum-Like Efficient Electrocatalyst for Hydrogen Evolution Reaction at All PH: Single-Crystal Metallic Interweaved V8C7 Networks. *Advanced Energy Materials* **2018**, *8* (23), 1800575.

(24) Chang, B.; Yang, J.; Shao, Y.; Zhang, L.; Fan, W.; Huang, B.; Wu, Y.; Hao, X. Bimetallic NiMoN Nanowires with a Preferential Reactive Facet: An Ultraefficient Bifunctional Electrocatalyst for Overall Water Splitting. *ChemSusChem* **2018**, *11* (18), 3198–3207. https://doi.org/10.1002/cssc.201801337.

(25) Hu, C.; Zhang, L.; Zhao, Z.-J.; Li, A.; Chang, X.; Gong, J. Synergism of Geometric Construction and Electronic Regulation: 3D Se-(NiCo)Sx/(OH)x Nanosheets for

Highly Efficient Overall Water Splitting. *Adv. Mater.* n/a-n/a. https://doi.org/10.1002/adma.201705538.

(26) Mishra, I. K.; Zhou, H.; Sun, J.; Qin, F.; Dahal, K.; Bao, J.; Chen, S.; Ren, Z. Hierarchical CoP/Ni5P4/CoP Microsheet Arrays as a Robust PH-Universal Electrocatalyst for Efficient Hydrogen Generation. *Energy Environ. Sci.* **2018**, *11* (8), 2246–2252. https://doi.org/10.1039/C8EE01270A.

(27) Meng, H.; Zhang, W.; Ma, Z.; Zhang, F.; Tang, B.; Li, J.; Wang, X. Self-Supported Ternary Ni–S–Se Nanorod Arrays as Highly Active Electrocatalyst for Hydrogen Generation in Both Acidic and Basic Media: Experimental Investigation and DFT Calculation. *ACS Appl. Mater. Interfaces* **2018**, *10* (3), 2430–2441. https://doi.org/10.1021/acsami.7b14506.

(28) Li, Y.; Tan, X.; Chen, S.; Bo, X.; Ren, H.; Smith, S. C.; Zhao, C. Processable Surface Modification of Nickel-Heteroatom (N, S) Bridge Sites for Promoted Alkaline Hydrogen Evolution. *Angewandte Chemie* **2019**, *131* (2), 471–476.

(29) Feng, J.-X.; Wu, J.-Q.; Tong, Y.-X.; Li, G.-R. Efficient Hydrogen Evolution on Cu Nanodots-Decorated Ni3S2 Nanotubes by Optimizing Atomic Hydrogen Adsorption and Desorption. *J. Am. Chem. Soc.* **2018**, *140* (2), 610–617. https://doi.org/10.1021/jacs.7b08521.

(30) Cai, Z.; Wu, A.; Yan, H.; Xiao, Y.; Chen, C.; Tian, C.; Wang, L.; Wang, R.; Fu, H. Hierarchical Whisker-on-Sheet NiCoP with Adjustable Surface Structure for Efficient Hydrogen Evolution Reaction. *Nanoscale* **2018**, *10* (16), 7619–7629.

(31) Yu, L.; Zhou, H.; Sun, J.; Qin, F.; Yu, F.; Bao, J.; Yu, Y.; Chen, S.; Ren, Z. Cu Nanowires Shelled with NiFe Layered Double Hydroxide Nanosheets as Bifunctional Electrocatalysts for Overall Water Splitting. *Energy & Environmental Science* **2017**, *10* (8), 1820–1827. https://doi.org/10.1039/C7EE01571B.

(32) Jiang, N.; You, B.; Sheng, M.; Sun, Y. Electrodeposited Cobalt-Phosphorous-Derived Films as Competent Bifunctional Catalysts for Overall Water Splitting. *Angewandte Chemie* **2015**, *127* (21), 6349–6352. https://doi.org/10.1002/ange.201501616.

(33) Du, C.; Yang, L.; Yang, F.; Cheng, G.; Luo, W. Nest-like NiCoP for Highly Efficient Overall Water Splitting. *Acs Catalysis* **2017**, *7* (6), 4131–4137.

(34) Gong, M.; Zhou, W.; Kenney, M. J.; Kapusta, R.; Cowley, S.; Wu, Y.; Lu, B.; Lin, M.-C.; Wang, D.-Y.; Yang, J. Blending Cr2O3 into a NiO–Ni Electrocatalyst for Sustained Water Splitting. *Angewandte Chemie International Edition* **2015**, *54* (41), 11989–11993.

(35) Gong, M.; Zhou, W.; Tsai, M.-C.; Zhou, J.; Guan, M.; Lin, M.-C.; Zhang, B.; Hu, Y.; Wang, D.-Y.; Yang, J.; Pennycook, S. J.; Hwang, B.-J.; Dai, H. Nanoscale Nickel Oxide/Nickel Heterostructures for Active Hydrogen Evolution Electrocatalysis. *Nature Communications* **2014**, *5*, 4695. https://doi.org/10.1038/ncomms5695.

(36) Tan, Y.; Wang, H.; Liu, P.; Shen, Y.; Cheng, C.; Hirata, A.; Fujita, T.; Tang, Z.; Chen, M. Versatile Nanoporous Bimetallic Phosphides towards Electrochemical Water Splitting. *Energy & Environmental Science* **2016**, *9* (7), 2257–2261. https://doi.org/10.1039/C6EE01109H.